Research paper

Numerical investigations of ship hydroelasticity of a 20,000 TEU containership based on CFD-MBD method

Wenjie Zhang [a], Jianhua Wang [a,*] , Hao Guo [b], Yi Liu [b], Decheng Wan [a]

[a] *Computational Marine Hydrodynamics Lab (CMHL), School of Ocean and Civil Engineering, Shanghai Jiao Tong University, Shanghai, 200240, China*
[b] *Marine Design and Research Institute of China, Shanghai, 200011, China*

ARTICLE INFO

ABSTRACT

In this paper, a fully coupled fluid-structure interaction method is proposed to study ship hydroelastic responses. A two-way coupling of CFD (Computational Fluid Dynamics) and MBD (Multi-Body Dynamics) solvers is applied to the numerical study of a 20,000 TEU containership. The flow field is solved using the RANS equations in OpenFOAM, while the structural dynamic responses are calculated using a beam model in MBDyn. Another open-source library, preCICE, is utilized for data exchange between the fluid and structural components in the coupling algorithm. The numerical results for the Response Amplitude Operators (RAOs) of ship motion and vertical bending moment (VBM) at midship are validated against experimental data under different wavelengths. Additionally, the hydroelastic responses are analyzed. The longitudinal distribution trends of the VBM under different wavelengths show a consistent pattern, with maximum hogging and sagging values occurring around the midship area. The maximum VBM responses are observed under conditions of $\lambda/L = 0.8$ and $\lambda/L = 0.9$, exhibiting significant high-frequency harmonic components. The comparison between numerical predictions of VBM for elastic and rigid ship body structures reveals a significant underestimation of VBM for rigid ships, even in relatively low sea conditions. This finding demonstrates the necessity of considering elasticity in the calculations of hydroelastic responses for ultra-large container ships.

1. Introduction

The prediction of hull structural strength is essential for the design of oceangoing ships in marine engineering, with ship seakeeping performance remaining a primary research focus. As modern ships grow larger and lighter, hydroelastic responses have become increasingly important in ship design, particularly for large-scale vessel types such as Ultra Large Container Ships (ULCS). Incidents involving container ships like the Napoli and Comfort emphasize the critical need for continued safety assessments in ship structural design, highlighting a vital area for further academic investigation. The rise of ULCS presents a new challenge in ship design, as their size exceeds the limits of classification of society rules and experience. This demonstrates the need to establish a new database for ULCS design, incorporating both experimental measurements and numerical simulations.

Since the introduction of two-dimensional strip theory for studying ship seakeeping performance in the 1970s (Korvin-Kroukovsky and Jacobs, 1957; Salvesen, 1970), the field has expanded to include two-dimensional hydroelastic theory for analyzing symmetric and antisymmetric responses of elastic hulls (Betts et al., 1977). Later, Bishop and Price (1979) the strip theory to predict the wave responses of two-dimensional ships considering the influence of the elasticity of ships. Since then, the numerical methods to predict the seakeeping performance and hydroelastic responses of ships based on potential flow theory have been developed and enriched greatly. Gu et al. (1989) proposed a time-domain formulation to calculate the nonlinear hydrodynamic loading of a slender ship with arbitrary heave motions. Wu et al. (1997) extended the unified slender body theory presented by Newman (1978), which is able to compute the distortion transformation of the ship body. In the fluid-structure interaction simulations between two-dimensional membrane structures and waves, Fukasawa (1990) added the nonlinear structural strain and displacement relations to predict the large deformations of the membrane structures. Hermundstad et al. (1994, 1999) developed the hydroelastic analysis method by adding one speed term to the linear free surface in the simulation of high-speed ships, which is proposed by Faltinsen and Zhao (1991).

With the rapid advancement of two-dimensional hydroelastic computational theories based on the symmetric and antisymmetric
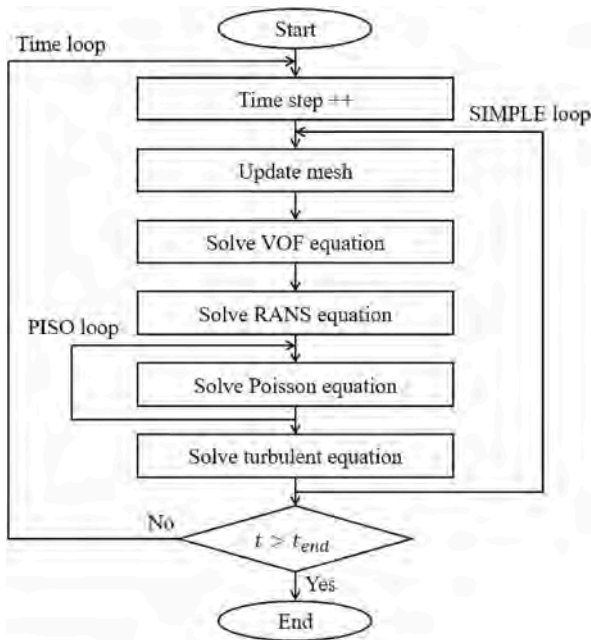
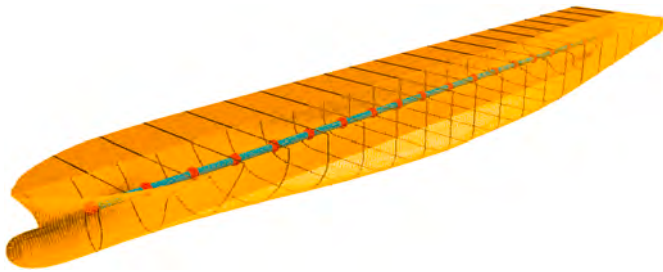**Fig. 1.** Flowchart of the fluid solver in OpenFOAM.

Fig. 2. Relationships between hull girder and sections.

characteristics of ships, three-dimensional hydroelastic methods grounded in potential flow theory have also been evolving. These methods were initially applied to the hydroelastic simulations of ellipsoid and smooth slender hulls (Faltinsen and Michelsen, 1975; Inglis, 1981). Price et al. (1985) further developed a three-dimensional hydroelastic theory incorporating generalized fluid-solid interface conditions, known as Price-Wu conditions, and applied this method to simulate the dynamic characteristics of a flexible SWATH structure.

Besides, the Morison approximation modification considering the viscous resistance of the fluid was introduced by Price and Wu (1989) to approximate the viscous influence of the fluid under the framework of potential flow. Wu et al. (1997) established a second-order nonlinear hydroelastic theory of three-dimensional floating bodies to analyze the effects of second-order wave loads on the floating structures. After a long period of development, the numerical hydroelastic computational method based on potential flow theory has formed a set of mature numerical prediction methods, which can consider the nonlinearity of fluid loads and structural characteristics to a certain extent. However, the solution based on the potential flow theory is difficult to escape the basic assumption of non-viscosity and non-vortex of the flow field, making it hard to simulate the phenomena of flow separation, fluid splashing and water accumulation.

There are connatural advantages by using CFD to simulate the flow field with high computational accuracy on nonlinear fluid behaviors than by using potential flow theory. With the great improvement of computing power of computers, the flow field calculation using CFD method has been widely used by scholars and engineers in the field of interactions between ship and waves (Wang et al., 2017, 2018). Besides, the coupling interactions only act on the interface between water and ships. It means the partitioned FSI coupling algorithm to calculate fluid domain and structure domain independently with different solvers is viable. This is conducive to make full use of the computational accuracy advantages of the existing solvers to carry out secondary development and to build a fluid-structure coupling solution framework for ship hydroelasticity problems. Over the past two decades, many scholars have carried out relevant research work. Oberhagemann et al. (2008, 2012) calculated the elastic structure deformation of a ship induced by waves by using a Timoshenko hull beam model based on the CFD-FEM coupling method. The rigid body motions of the ship were linearly superimposed on elastic hull deformations to update the mesh of flow field domain. The reliability of the proposed fluid-structure coupling method was verified by the comparisons with the experimental results of the motion and VBM loads of a 13,000TEU and a 7,500TEU container ship. Paik et al. (2009) proposed a numerical calculation method based on the principle of modal superposition to calculate the structural hydroelastic responses of ships in waves and applied it to study the influence of ship elasticity on bow slamming and VBM. In addition, one-way coupling algorithm without considering the influence of the ship's elastic deformation on the flow field mesh is applied and the simulation results are compared with that by using two-way coupling algorithm which takes the influence into account. The one-way coupled approach with a virtual mass correction is provided to correct the influence of fluid-structure interactions due to the updating of the mesh. Seng (2012) developed a FSI program to calculate ship's seakeeping performance and hydroelastic response in waves based on CFD-FEM
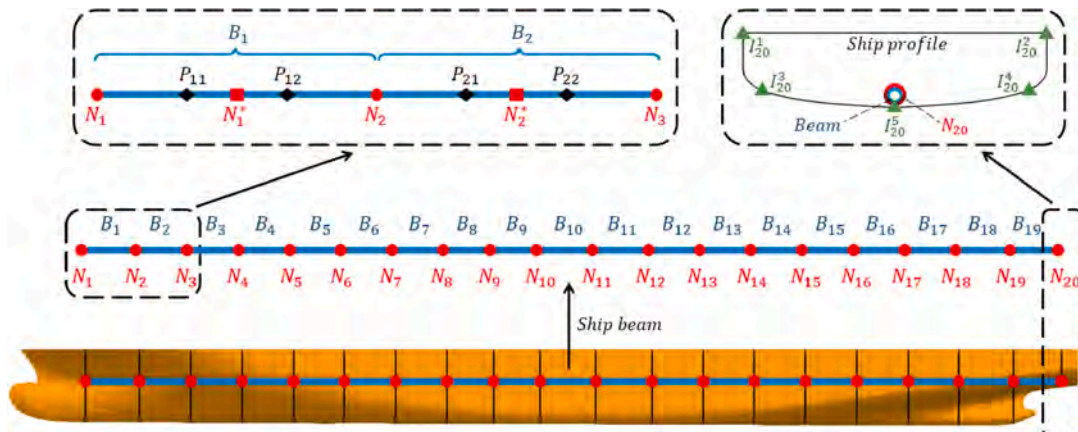

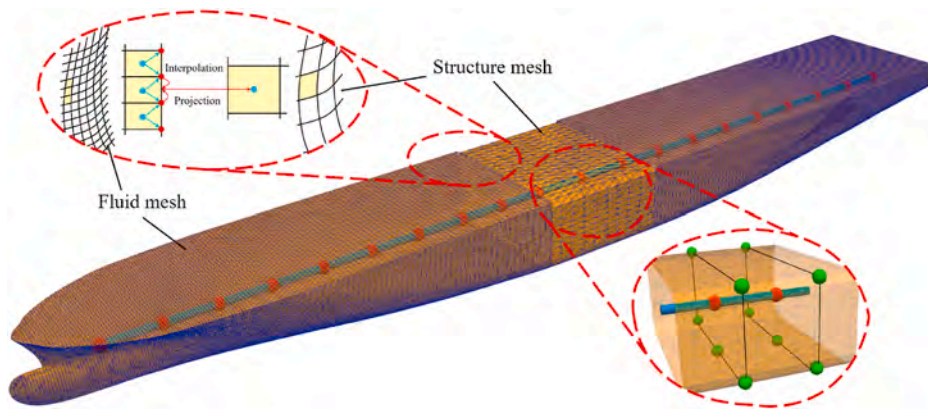**Fig. 3.** Diagram of a three-node beam and interpolation points.

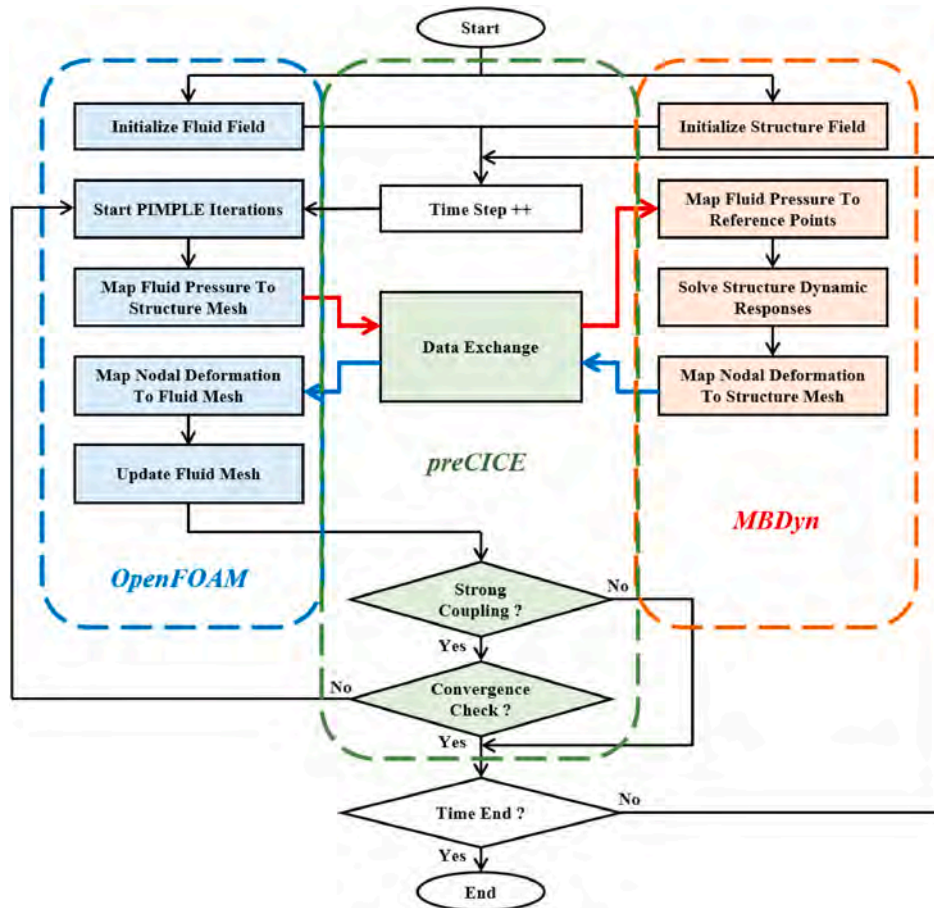**Fig. 4.** Relation between fluid mesh, structure mesh, and hull beam.

Fig. 5. Framework of the fluid-structure coupling.

coupling method. Based on the data from model test of a 9400 TEU container ship, the calculation accuracy of the developed solver was validated. The structural responses of amidship VBM of hull girder due to bow flare slamming is studied. In addition to the development of in-house code, there is also a lot of work of ship hydroelastic numerical simulations based on commercial software and open-source code that have been built the simulation platform of FSI.

In recent years, it has become a common method to forecast ship motions, wave loads and VBM responses in waves by using the coupling of commercial software. Huang et al., 2022, Yang et al., 2021 and Jiao et al., 2021, Takami and Iijima, 2020 independently carried out a number of numerical simulations based on the container ship S-175 with

STAR-CCM+ and Abaqus and validated the computational accuracy of the prediction results of the ship's seakeeping performance and hydroelastic response compared with experimental data and enriched the data set of S-175 ship models. Liu (2021) validated the numerical prediction results of ship motions and VBM responses of a 6750 TEU container ship, with the experimental data from Korea Institute of Shipping and Ocean Engineering (KRISO) by using STAR-CCM+ and Abaqus. Based on STAR-CCM+ and LS-DYNA, Wei et al., 2022, Takami et al., 2018 compared the simulation results of local double-bottom bending moment (DBM) responses by using one-way coupling, two-way loose coupling and two-way tight coupling approach for a 6, 600TEU ship model. The effects of the hydroelastic component in DBM

Table 1
Principal particulars of the 20,000 TEU containership.

Main particular	Symbol	Full scale	Model
Scale	μ	1:1	1:49
Length between perpendiculars	L_{PP} (m)	383.0	7.816
Breadth	B (m)	58.6	1.196
Depth	D (m)	30.5	0.622
Fore draught	d_F (m)	15.2	0.310
After draught	d_A (m)	16.7	0.341
Displacement	Δ (t)	2.58×10^5	2.161
Block coefficient	C_B	0.69	0.69
Centre of gravity longitudinal center of gravity (LCG) from aft perpendicular (AP)	X_g (m)	182.7	3.729
Vertical center of gravity (KG) from base line	Z_g (m)	27.6	0.563
Moment of inertia about y-axis	I_{yy} (kg·m²)	2.307×10^{12}	7967.86

on the total DBM and hull girder ultimate strength were studied. In addition to commercial software, there is also some researches on ship hydroelasticity by using open-source code in recent years. Wei et al. (2023, 2024) applied the CFD solver, OpenFOAM, and the structural dynamic solver MBDyn, constituting a two-way FSI coupling solver based on CFD-DMB method. The hydroelastic response of the intact and damaged hull structures of the S-175 container ship model under regular head waves is compared. However, the FSI coupling procedure of the studies of Wei is based on the in-house code and others are based on the commercial software, which make it very hard for the promotion and further development of technology.

In this study, a two-way coupling CFD-MBD method is proposed and applied to the numerical simulations of seakeeping performance and hedroelastic analysis of a 20,000 TEU containership by using open-source FSI coupling library preCICE. It filled the gap on the application of three-node beam model to ULCS with open-source FSI coupling code. The flow field is solved by OpenFOAM solver, and the structural response of the hull girder is solved by MBDyn. The data exchange between the two solvers and convergence check in the FSI simulation are performed by preCICE. The prediction results are validated against the experimental data. The effect of wavelength and structural stiffness on ship motion and VBM responses are also discussed.

2. Numerical approach

In this section, we propose a two-way coupled CFD-MBD method for the numerical prediction of ship hydroelastic responses. The fluid
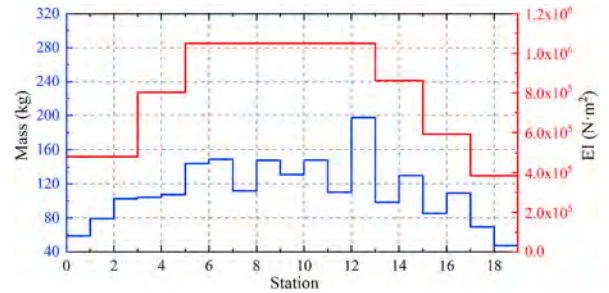

Fig. 8. Longitudinal mass and vertical bending stiffness distribution of the hull in model scale.
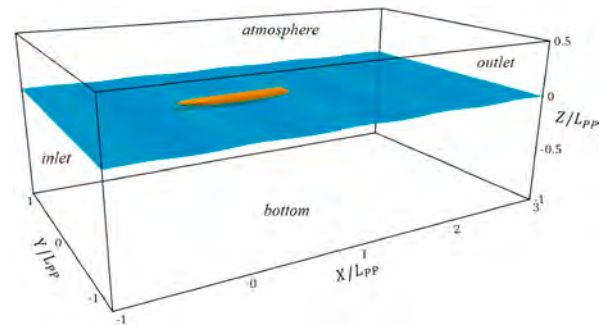

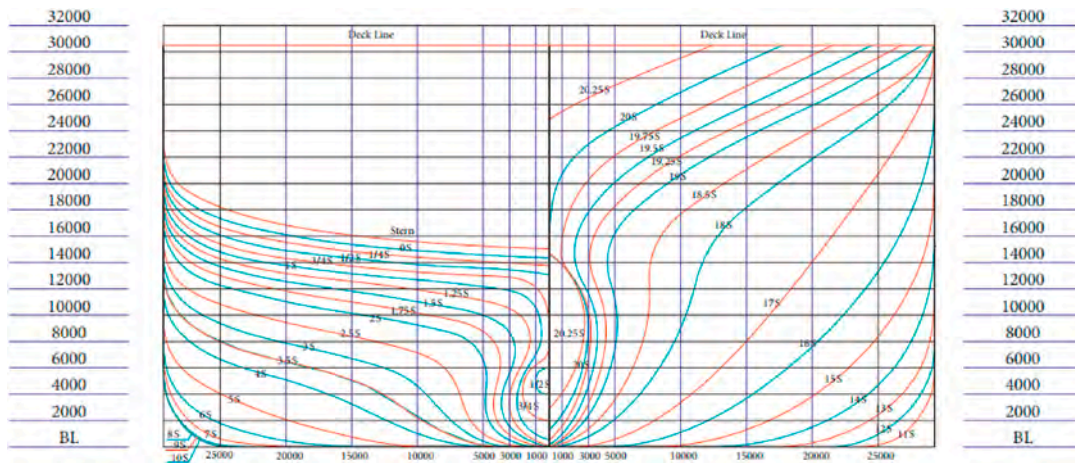**Fig. 9.** General view of the numerical computational domain.

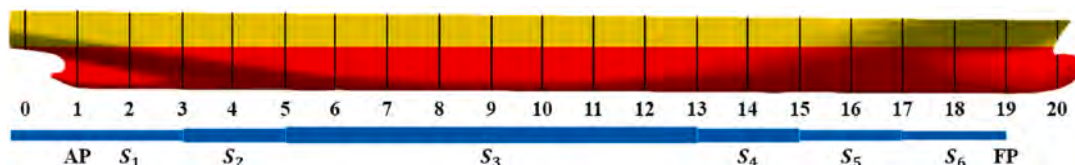**Fig. 6.** Body lines of 20,000 TEU containership (Lu et al., 2022).
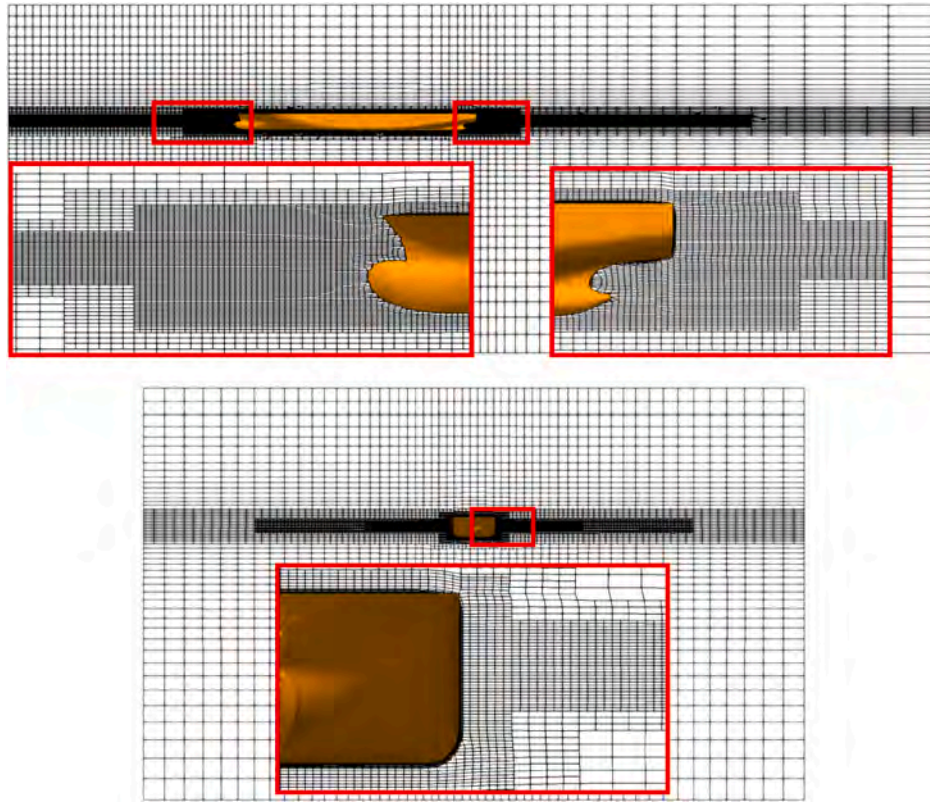

Fig. 7. Arrangement of ship segments and hull girder.

Fig. 10. Mesh details around the hull.

Table 2
Simulation conditions in this study.

Case ID	Wavelength (λ/L)	Wave frequency (ω, rad/s)	Encounter frequency (ω_e, rad/s)	Wave steepness (H/λ)
1	0.7	3.356	4.813	0.0186
2	0.8	3.140	4.414	0.0163
3	0.9	2.960	4.092	0.0145
4	1.0	2.808	3.828	0.0131
5	1.1	2.677	3.604	0.0119
6	1.2	2.563	3.413	0.0109
7	1.3	2.463	3.247	0.0100
8	1.4	2.373	3.101	0.0093
9	1.5	2.293	2.972	0.0087

dynamics are solved using OpenFOAM, while the structural calculations are performed using a hull girder model in MBDyn. The fluid-structure interaction data is updated through the open-source FSI library, pre-CICE. The details of this coupling approach are elaborated below.

2.1. Fluid solver

The two-phase, incompressible flow field is solved by transient CFD solver interFoam in the open-source hydrodynamic code OpenFOAM:

Table 3
Calibrated beam natural frequency of model vertical bending modes.

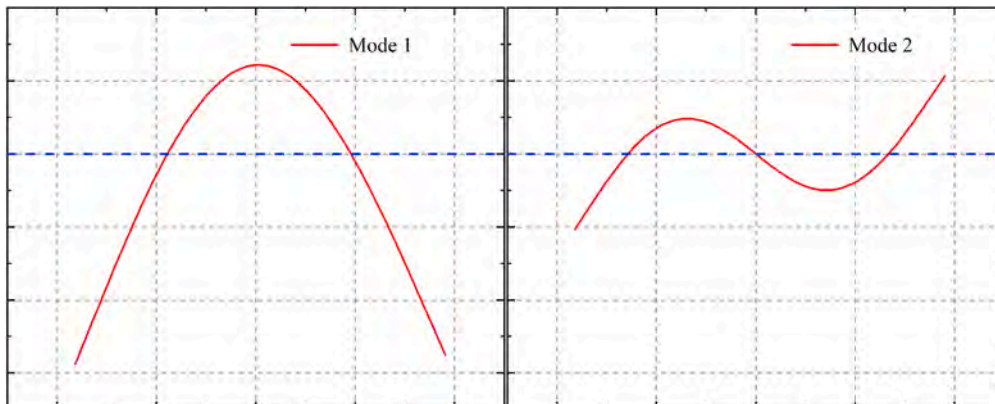| Order	Mode	f_{MBD} (Hz)	f_{exp} (Hz)	Error
1st	2	3.869	3.823	1.20%
2nd	3	8.822	8.575	2.88%

Fig. 11. Natural mode of beam vertical bending vibration in the 2-node and 3-node order.

Table 4
Grid information for the verification studies.

Grid Level	Cell Number (million)
Coarse	3.37
Medium	4.07
Fine	5.93

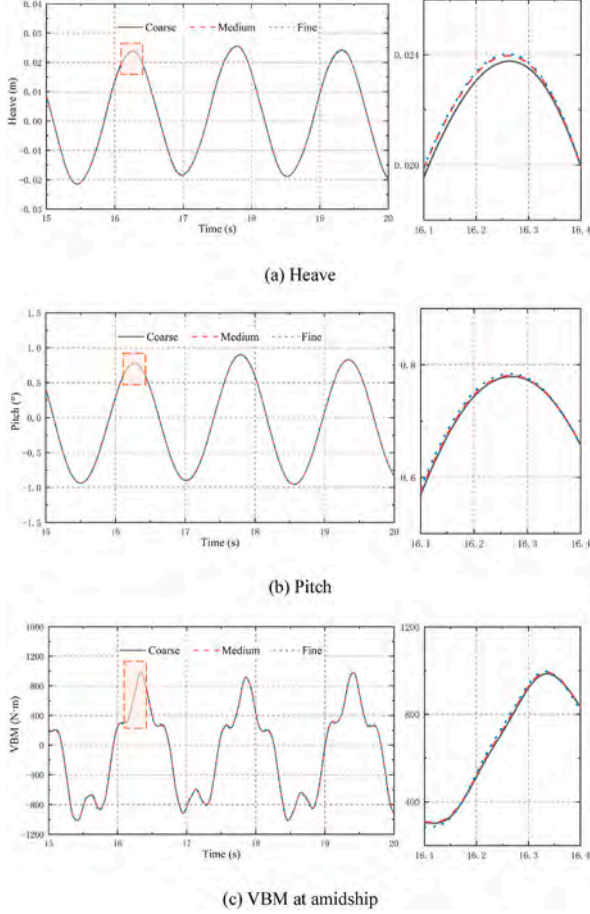(a) Heave

(b) Pitch

(c) VBM at amidship

Fig. 12. Time series of ship motions and amidship VBM of different mesh level.

Table 5
Results of convergence study of different grid levels.

Parameters		Values		
Description	Symbol	Heave (mm)	Pitch (deg)	VBM (kNm)
Fine mesh	S_1	24.020	0.784	0.996
Medium mesh	S_2	23.963	0.781	0.993
Coarse mesh	S_3	23.760	0.778	0.985
Convergence rate	R	0.282	0.900	0.417
Convergence type	/	MC	MC	MC
Precision	P	3.654	0.304	2.526
Extrapolated values	$S_{ext.32}$	0.024	0.808	0.998
Approximate relative error	$e_{a.32}$	0.846%	0.384%	0.732%
Extrapolated relative error	$e_{ext.32}$	0.331%	3.342%	0.521%
Grid convergence index	GCI	0.004	0.043	0.007
Uncertainty	U	0.004	0.043	0.007

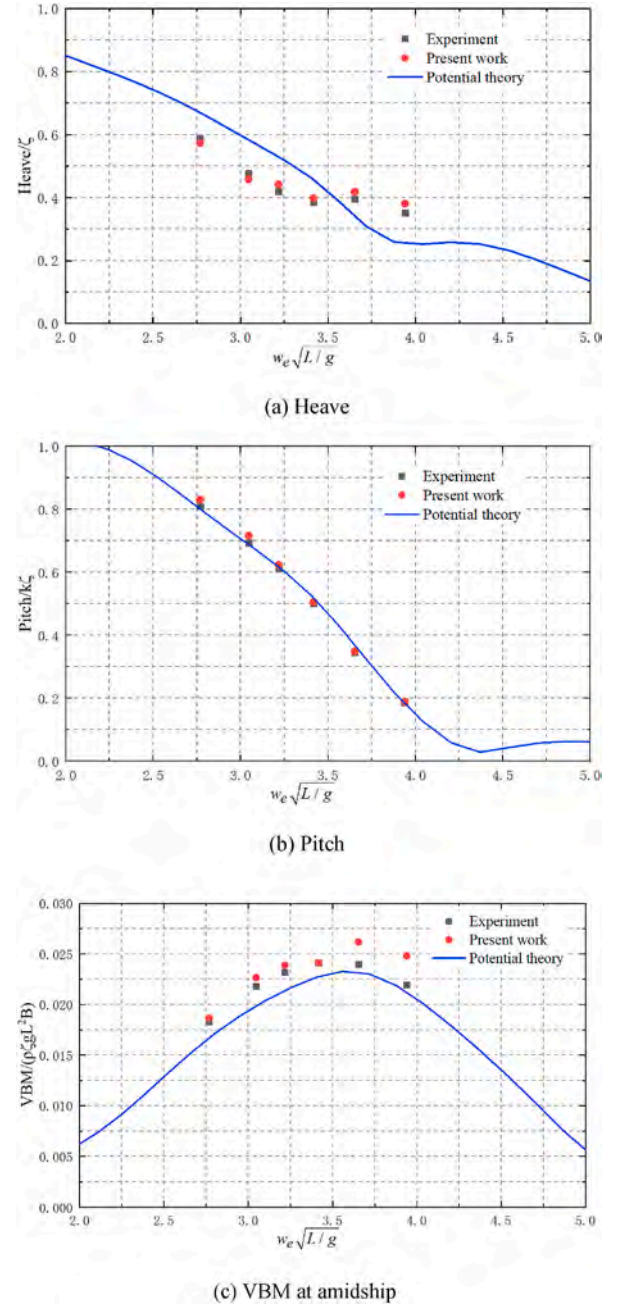(a) Heave

(b) Pitch

(c) VBM at amidship

Fig. 13. Comparison of RAOs of motions and VBM at amidship.

$$\nabla \cdot \boldsymbol{U} = 0 \tag{1}$$

$$\frac{\partial(\rho \boldsymbol{U})}{\partial t} + \nabla \cdot (\rho \boldsymbol{U}\boldsymbol{U}) = -\nabla p + \nabla^2(\rho \mu \boldsymbol{U}) + \rho \boldsymbol{g} \tag{2}$$

where $\boldsymbol{U}$ is the field velocity vector, p is the pressure, and $\boldsymbol{g}$ is the acceleration vector due to gravity. And the fluid density, ρ, and the kinematic viscosity, μ, are determined using the Volume Of Fluid (VOF) interface capturing scheme (Rusche, 2002):

$$\frac{\partial \alpha}{\partial t} + \nabla \cdot (\alpha \boldsymbol{U}) + \nabla \cdot [\alpha(1-\alpha)\boldsymbol{U_r}] = 0 \tag{3}$$

$$\rho = \rho_{air}(1-\alpha) + \rho_{water}\alpha \tag{4}$$

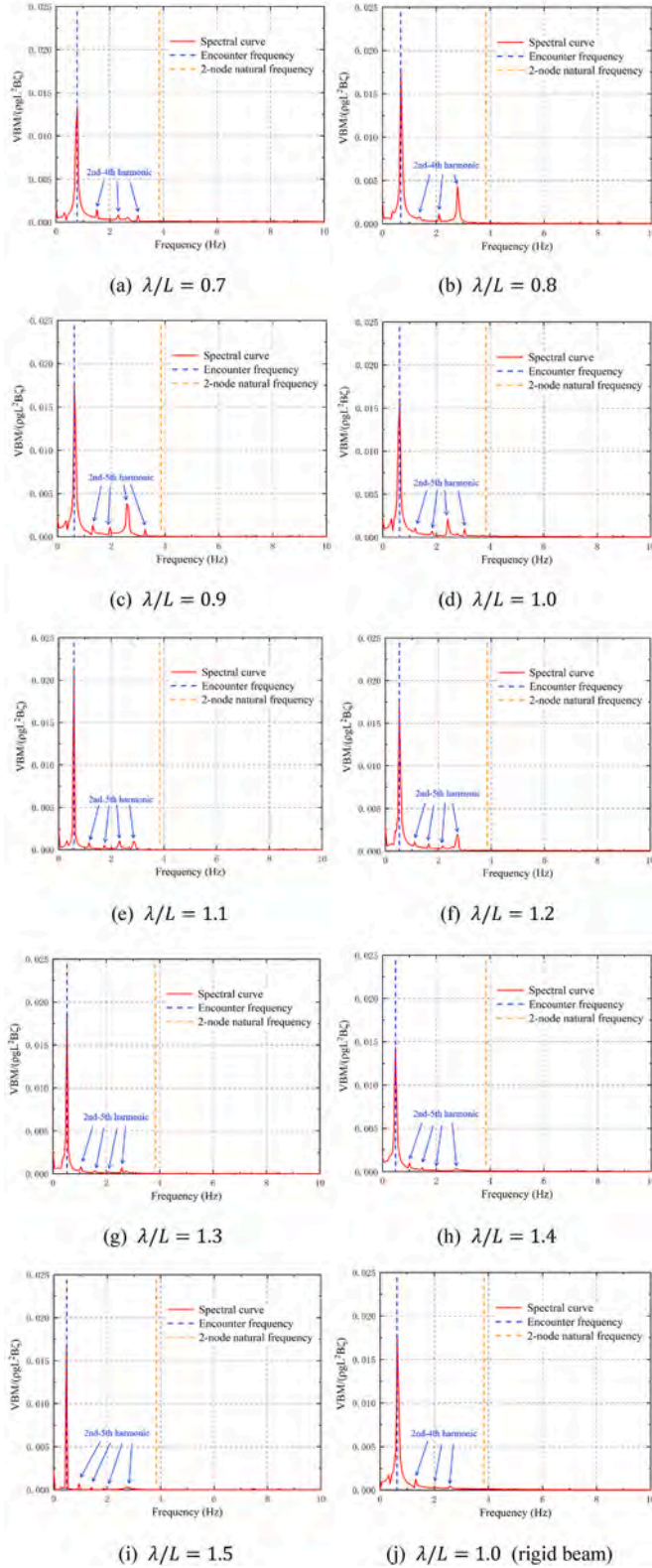$$\mu = \mu_{air}(1-\alpha) + \mu_{water}\alpha \tag{5}$$

Fig. 14. Spectra of VBM amidships for different wavelength ($\lambda / L = 0.7 \sim 1.5$).

where α is the volume of fraction, 0 and 1 represent that the mesh cell is filled with air and water, respectively. $\boldsymbol{U_r}$ is the velocity vector used to compress the interface. The regular head waves are generated by velocity inlet boundary conditions (Wang et al., 2019). The $k-\omega$ SST model is used to solve the turbulence in this simulation. The turbulent

kinetic energy k and the specific dissipation rate ω are given as:

$$\frac{\partial k}{\partial t} + \nabla \cdot (\boldsymbol{U} k) = \widetilde{G} - \beta^* k \omega + \nabla \cdot [(\nu + \alpha_k \nu_t) \nabla k] \tag{6}$$

$$\frac{\partial \omega}{\partial t} + \nabla \cdot (\boldsymbol{U} \omega) = \gamma S^2 - \beta \omega^2 + \nabla \bullet [(\nu + \alpha_\omega \nu_t) \nabla \omega] + (1 - F_1) CD_{k\omega} \tag{7}$$

where F_1 is a mixed function combing the models of $k - \omega$ and $k - \varepsilon$:

$$F_1 = \tanh \left\{ \min \left[\max \left(\frac{\sqrt{k}}{\beta^* \omega y}, \frac{500\nu}{y^2 \omega} \right), \frac{4\alpha_{\omega 2} k}{CD_{k\omega}^* y^2} \right] \right\}^4 \tag{8}$$

More details can be found in the work of Menter (1994). The PIMPLE algorithm applied in OpenFOAM is a combination of PISO (Pressure Implicit with Splitting of Operators) and SIMPLE (Semi-Implicit Method for Pressure-Linked Equations) to decouple the velocity and pressure, as shown in Fig. 1. For this simulation, the schemes of Euler, Total Variational Diminishing (TVD) and central differential are applied in the computation of temporal, convection and diffusion terms, respectively. Besides, a Gaussian method is used for gradient reconstruction and a linear profile is applied for variable face interpolation.

To update the flow field mesh because of structural deformation, the dynamic mesh motion solver displacementLaplacian is applied in OpenFOAM. After obtaining the hull deformation results from structure solver, the final step is to propagate the displacement deformation in the boundary field into the internal volume mesh. The displacement field δX is solved by Laplacian's equation:

$$\nabla \cdot (\gamma \nabla (\delta X)) = 0 \tag{9}$$

where γ is a diffusion coefficient, as a constraint to increase the solution smoothness. In this study, a quadratic function of the inverse distance from the boundary is applied, meaning $\gamma = 1/r^2$ and r is the distance from internal cell centers to structural boundaries.

2.2. Structure solver

In this study, the structural dynamic response of the hull girder is computed by MBDyn, an open-source multibody dynamic solver (Masarati et al., 2014). In the structural calculation, the ship is simplified as an elastic hull girder, representing its geometric characteristics and mass distribution. The girder is divided into different sections with specific mass and stiffness attributes. In the coupling calculation with the flow field, the surface mesh on the hull transfers the interpolated flow field pressure to the related girder nodes for the computation of hull motion and elastic deformation. Fig. 2 illustrates the relationship between a hull girder and the sections.

The red dots in Fig. 2 represent nodes on the hull girder, where the displacement and velocity are calculated at each time step. The Newton-Euler equations of motion for each node and constrained equations are written in differential-algebraic form as (Simeon, 2006):

$$M\dot{\boldsymbol{x}} = \boldsymbol{p} \tag{10}$$

$$\dot{\boldsymbol{p}} + \phi_x^T \lambda = f(\boldsymbol{x}, \dot{\boldsymbol{x}}, t) \tag{11}$$

$$\phi(\boldsymbol{x}, t) = 0 \tag{12}$$

where M is the inertial matrix of the rigid body; x is the translational and rotational nodal coordinates in global system; p denotes the momentum vector of the body; ϕ denotes a set of kinematic constrains applied on the body and ϕ_x^T is the Jacobian matrix of ϕ; the Lagrange multipliers vector, λ, representing algebraic constraints reactions explicitly applied to motion equations; f denotes the external force and moment. Moreover, the positioning of ship model in waves is also set in the structure solver. In this study, the bow node of the hull beam is selected as a fixed point connected with the global coordinate system. The motions along the

Table 6

Details of RAO comparison of ship motion and VBM at amidship.

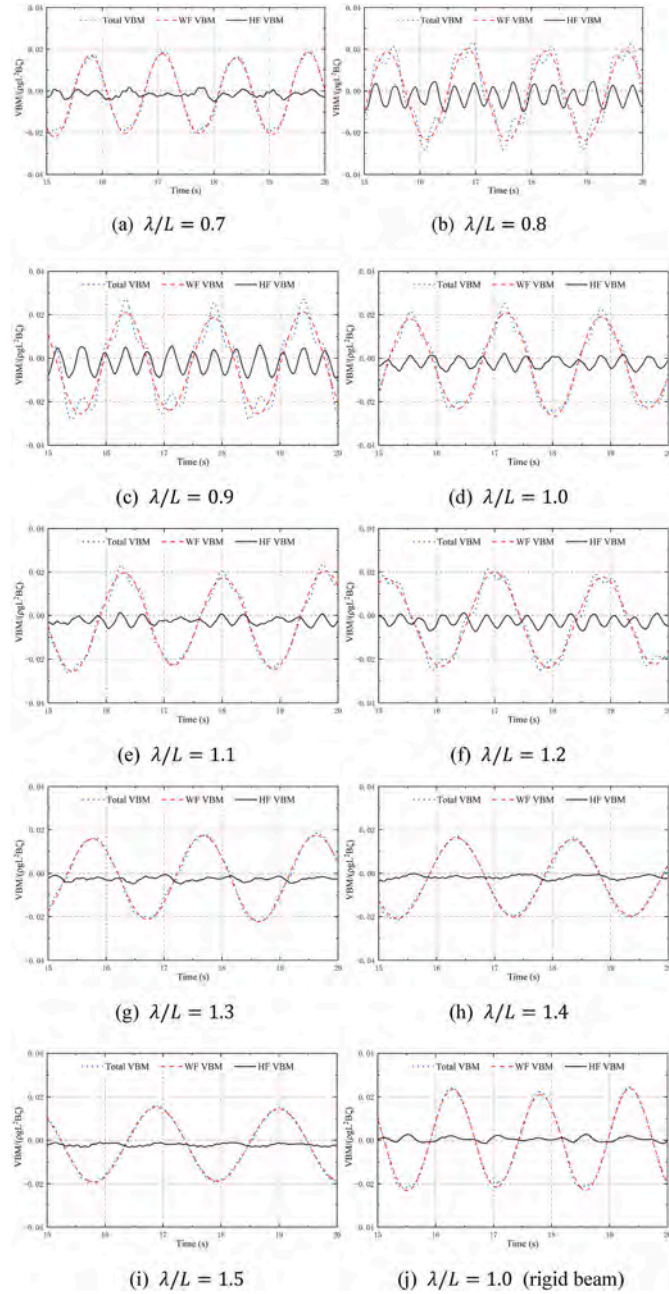| Wavelength (λ/L)	Heave/ ζ			Pitch/($k\zeta$)			VBM/($\rho\zeta gL^2B$)		
	Num	Exp	Error	Num	Exp	Error	Num	Exp	Error
0.8	0.381	0.351	8.5%	0.190	0.186	2.2%	0.0248	0.0220	12.7%
0.9	0.418	0.395	5.8%	0.349	0.347	0.6%	0.0262	0.0240	9.2%
1.0	0.398	0.385	3.4%	0.506	0.502	0.8%	0.0241	0.0241	0.1%
1.1	0.442	0.419	5.5%	0.623	0.612	1.8%	0.0239	0.0232	3.9%
1.2	0.458	0.478	−4.2%	0.717	0.694	3.3%	0.0227	0.0218	4.1%
1.4	0.573	0.587	−2.4%	0.831	0.810	2.6%	0.0187	0.0183	2.2%

Fig. 15. Time histories of VBM components at amidships for different wavelength (λ/L = 0.7–1.5).

length and width directions of the ship are limited at this node to guarantee the position of the ship to be stable in waves. While the motions of heave and pitch are set as free on the node, which plays the same

Table 7

Comparisons of the amplitude values and component proportions of WF and HF VBM components.

Wavelength (λ/L)	Amplitude of VBMs/($\rho\zeta gL^2B$)			Component proportion	
	WF	HF	Total	WF/Total	HF/Total
0.7	0.0183	0.0029	0.0194	94.3%	15.0%
0.8	0.0221	0.0059	0.0248	89.1%	23.8%
0.9	0.0225	0.0062	0.0262	85.9%	23.7%
1.0	0.0213	0.0034	0.0241	88.4%	14.1%
1.1	0.0223	0.0027	0.0239	93.3%	11.3%
1.2	0.0219	0.0026	0.0227	96.5%	11.5%
1.3	0.0198	0.0017	0.0200	99.0%	8.5%
1.4	0.0185	0.0013	0.0187	98.9%	7.0%
1.5	0.0171	0.0010	0.0174	98.3%	5.8%

effect in the towing trials as the fixed point in ship model.

In the structure part of MBDyn, a geometrically non-linear three-node beam is applied within a multibody frame (Ghiringhelli et al., 2000). The beam model is discretized as elements through a finite volume approach. As shown in Fig. 3, there are three reference points (red dots, like N_1, N_2 and N_1^*) and two evaluation points (black diamonds, like P_{11} and P_{12}) in each beam element (like B_1). External forces and moments are integrated over every beam element position related to reference points (green triangle, like I_{20}^i, $i = 1$–5), and internal forces and moments are calculated at the evaluation points. In the FSI coupling approach, hydrodynamic forces will be transformed into reference points to compute structural response. The process of data exchange between fluid part and solid part will be detailed below.

2.3. FSI coupling

A high-efficient open-source coupling library preCICE is applied in the two-way partitioned numerical simulation in the coupling procedure between fluid solver and structure solver. This library provides an effective platform for data coupling, mapping and communication. Especially, the calculation of both fluid domain and structure domain will be solved several times in one time step, until the residual settings are required. This procedure makes the coupling between fluid part and solid part tighter, leading to a strong coupling algorithm. The coupling library has been applied and validated in the previous work (Xiao et al., 2024).

In the strong coupling algorithm, the interface between the fluid and the structure is governed by the conditions of a kinematic interface condition (i.e. velocity continuity equation) and a dynamic interface condition (i.e. normal stress continuity equation):

$$U_f = U_s \tag{13}$$

$$p_f \cdot n_f = -\sigma_s \cdot n_s \tag{14}$$

where U_f and U_s are velocity vectors in the fluid and structure field, respectively. The p_f is the fluid pressure along the interface, σ_s is the structural stress tensor. n_f and n_s are the unit normal vectors along the interface in fluid domain and solid domain, respectively. In this study,
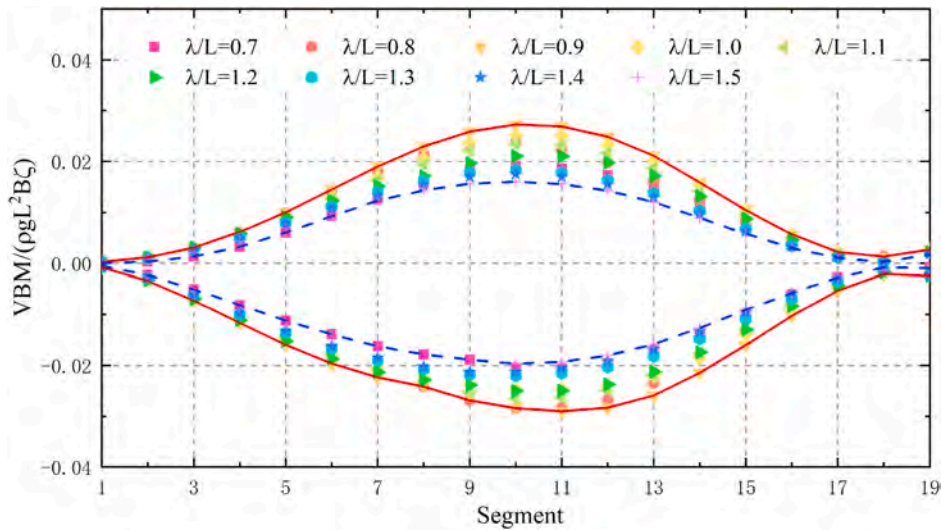
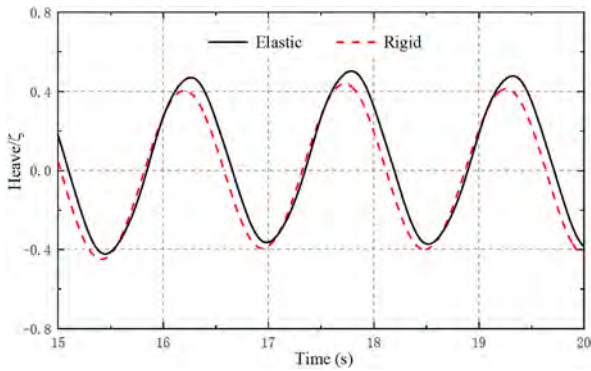**Fig. 16.** Longitudinal distribution of VBM for different wavelength ($\lambda/L = 0.7$–1.5).

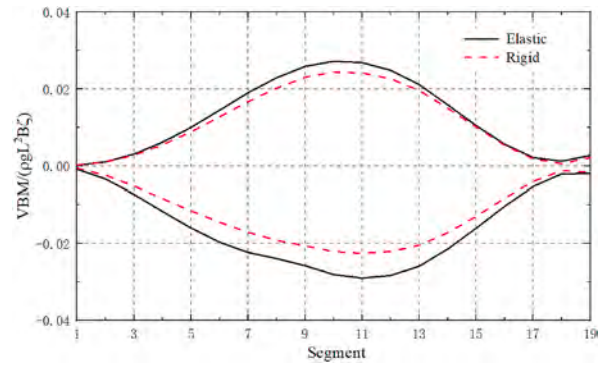**Fig. 17.** Comparison of heave motion between elastic and rigid beams ($\lambda/L = 0.9$).

Fig. 19. Comparison of longitudinal distribution of VBM between elastic and rigid beams ($\lambda/L = 0.9$).
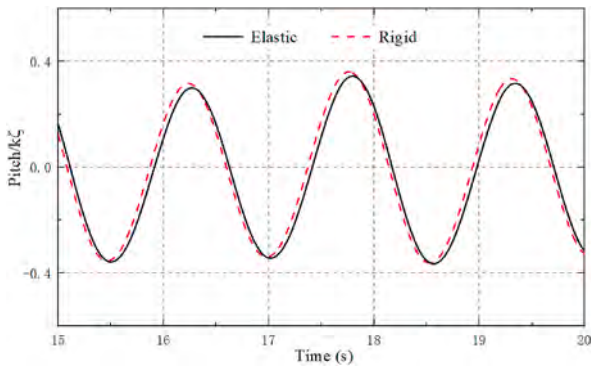

Fig. 18. Comparison of longitudinal distribution of VBM between elastic and rigid beams ($\lambda/L = 0.9$).

Table 8
RAO comparisons of ship motion and VBM at amidship between rigid and elastic ships.

	Rigid	Elastic	Difference
Heave/ ζ	0.405	0.418	−3.1%
Pitch/($k\zeta$)	0.352	0.349	0.8%
VBM/($\rho\zeta gL^2B$)	0.0228	0.0262	−13.0%

Fig. 20. Comparison of time series of VBM components at amidships between elastic and rigid beams ($\lambda/L = 0.9$).

the maximum number of iterations for fluid-structure coupling within one time step is defined as 20. The convergence residuals for structural deformation and flow field pressure are specified as 2e-4 and 2e-3, respectively.

The strong coupling algorithm is realized by a crucial detail of communications between fluid mesh and structure mesh, as shown in Fig. 4. Initially, the pressure distribution calculated by the flow field mesh on the hull surface is interpolated onto the grid nodes from cell center. Subsequently, hydrodynamic forces on the grid nodes in fluid
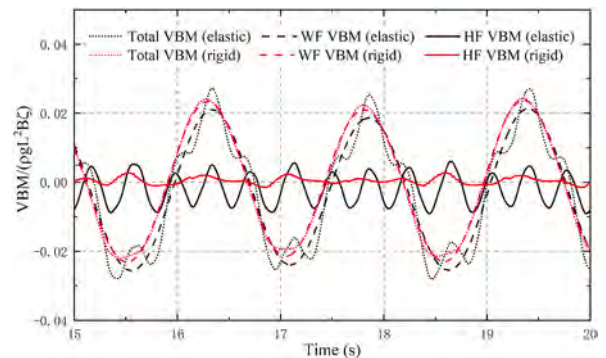
Table 9
RAO comparisons of VBM components at amidship between rigid and elastic ships.

VBM/$(\rho\zeta gL^2B)$	Rigid	Elastic	Difference
WF	0.0224	0.0221	1.4%
HF	0.0017	0.0063	−73.0%
Total	0.0228	0.0262	−13.0%

mesh are interpolated and projected to cell center of structure mesh by using a nearest-projection interpolation method. The fluid pressure acting on cell centers in the structure mesh are mapped onto the reference points mentioned above (green dots in Fig. 4). The mapping builds the relations of the displacement and velocity between the structure mesh (subscript "s") and the reference points (subscript "mbd") by a constant matrix H (MBDyn, 2017):

(a) $t/T_e = 10.36$

(b) $t/T_e = 10.59$

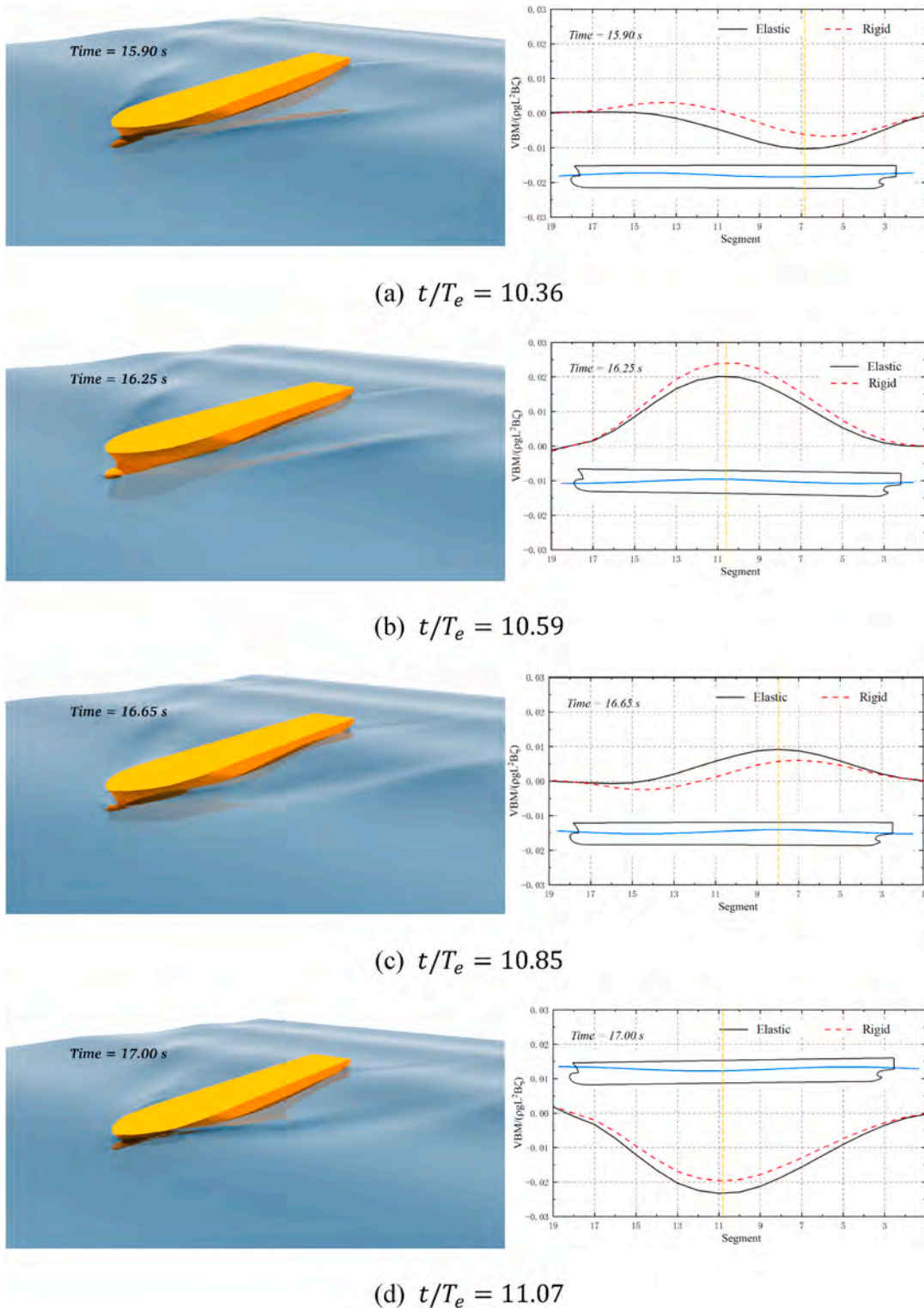(c) $t/T_e = 10.85$

(d) $t/T_e = 11.07$

Fig. 21. Elastic ship motion and longitudinal distribution of VBM in one wave encounter period ($\lambda/L = 0.9$).
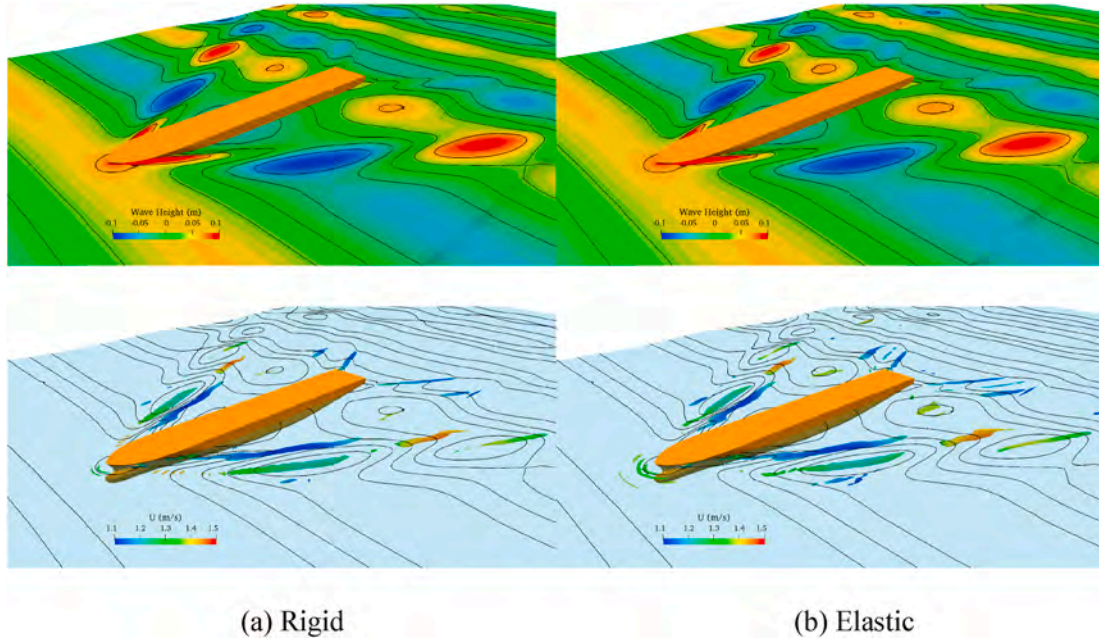
Fig. 22. Flow field and vortical structures around rigid and elastic ship (Time = 17.00 s, $\widetilde{\Omega}_R = 0.7$, $\lambda/L = 0.9$).

$$x_s = Hx_{mbd} \tag{15}$$

$$\dot{x}_s = H\dot{x}_{mbd} \tag{16}$$

And the matrix H is also applied in the force mapping with the conservation of the work done in two domains:

$$\delta x_s^T f_s = \delta x_{mbd}^T f_{mbd} = \delta x_{mbd}^T H^T f_s \tag{17}$$

which implies:

$$f_{mbd} = H^T f_s \tag{18}$$

A similar process is employed in transmitting structural deformation back to the flow field. Firstly, the deformations of beam nodes are interpolated onto the surface grid nodes of the hull structure and then mapped to the surface mesh of flow field using a nearest-projection interpolation method. After the grid distribution of the boundary position in the flow field is obtained, the internal grid node coordinates of the flow field are updated based on the dynamic mesh motion solver.

The two-way strong coupling procedure is shown in Fig. 5. Both solvers of fluid part and structure part are firstly initialized and go into the time step loop. In each time step, the flow field pressure distribution is solved and mapped onto the structure mesh of hull surface. The mesh nodal deformation distribution is solved and transferred back to the flow field after the computation of structural responses. The fluid mesh is updated then by solving the Laplacian's equation. Both fluid pressure and structural deformation residuals are checked for convergence to ensure the strong coupling. The calculation process in each time step loops until the specified final time is reached.

3. Numerical setups

3.1. Ship model description

In this study, the numerical settings are based on a 20,000 TEU containership model, and the experimental data are from model tests in CSSRC (China Ship Scientific Research Center). It is noted that only the naked model is involved for investigation without any appendages. The main particulars of the 20,000 TEU ship are listed in Table 1.

The body lines of the containership are shown in Fig. 6. And the

arrangement of hull girder is shown in Fig. 7, from forward perpendicular at station 19 to the stern of the ship. The beam is divided into 19 segments based on the position of stations. It is important to note that there are two hull girders symmetrically distributed around the middle longitudinal plane, and they have the same settings in the experiments. However, in this simulation, there is only one hull girder taken into computation. This is because that only vertical bending is considered while horizontal bending and torsion effects are ignored. In the tests, the moment of inertia of a simplified beam model is designed to be equivalent to the sum of the moments of inertia of two actual beams. Consequently, one simplified beam with an equivalent moment of inertia is employed in the structural computation. In Section 4.1, the natural frequency of vertical vibration of the simplified beam is validated to ensure that there is little influence made by this simplification in mass and stiffness distribution compared with the experimental setup.

The longitudinal mass and vertical bending stiffness distribution of the model is shown in Fig. 8. The hull beams of the ship model in the experiments are constructed by assembling six circular tubes with different cross-sectional sizes, as illustrated in Fig. 7. Consequently, the vertical bending stiffness distribution of the beam in the numerical simulations are composed of six distinct segments. In addition, to obtain a pronounced higher frequency (HF) hydroelastic responses of the ship model, the damping of the structure is set as zero in the simulations, which is consistent with the approach taken by Jiao et al. (2021).

The numerical calculations in this paper only consider head waves, thus the kinematic constraints on the hull structure are imposed by fixing the motion in surge, sway, roll and yaw directions on each beam node. This allows the ship with heave and pitch motions exclusively.

3.2. Numerical wave tank setup

Fig. 9 shows a general view of the flow field computational domain. The extent of the region is $-1\,L_{PP} < x < 3\,L_{PP}$, $-1.2\,L_{PP} < y < 1.2\,L_{PP}$, and $-1\,L_{PP} < z < 0.5\,L_{PP}$, where L_{PP} represents the ship length between perpendiculars. The mean free surface of the regular wave lies at z = 0. The wave suppression region starts from 2Lpp and ends to 3Lpp in the longitudinal direction. At the inlet boundary, the velocity boundary condition is set as specified wave and current, and the pressure is set as zero flux pressure. At the outlet boundary, the mean current velocity is set to make the mass conservation of flow field, and the pressure is set as
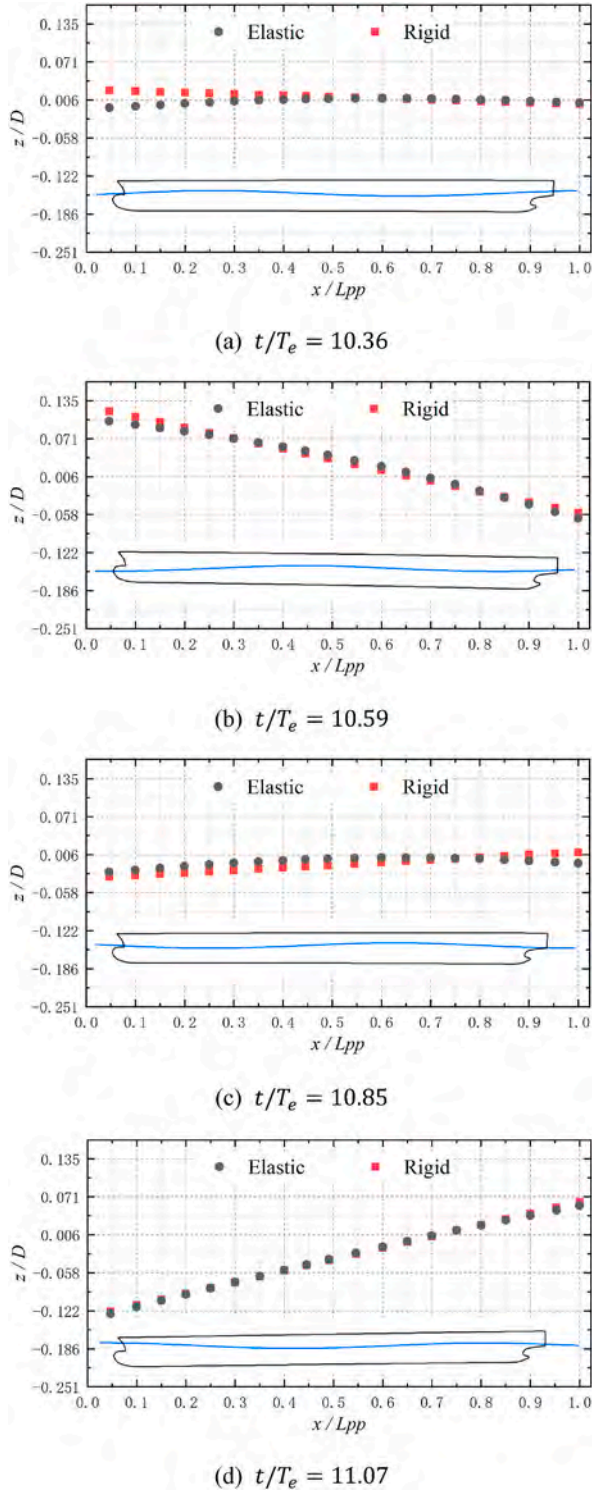
Fig. 23. Displacement distribution of structural nodes in one wave encounter period (λ/L = 0.9).

zero gradient. The bottom and hull surface are set as wall and moving wall boundary conditions, respectively. The top region of the computational domain is set as atmosphere with zero pressure and computed velocity. Besides, the left and right boundaries are set as symmetry planes.

The flow field domain is discretized and locally refined with block-Mesh and snappyHexMesh, the pre-processing tools in OpenFOAM, as illustrated in Fig. 10. The computational region around the hull and free

surface region are refined to satisfy the criterion of 10 cells per wave height and 170 cells per wavelength for the simulation condition with the shortest wavelength. The aspect-ratio of grids in the refinement regions are set as 3.0 and the total mesh number in this study is 4.07 million.

3.3. Computational conditions

A series of computation conditions are carried out for a systematic analysis of the seakeeping performance and hydroelastic responses of the containership. All the investigation conditions are simulated in head regular waves with the same wave height of 102 mm (full scale 5.0 m). The ship speed of Fr = 0.145 (full scale 17.25 knots) is applied to be in consistence with the value in the model tests. Table 2 summarizes the simulation conditions in this study.

4. Verifications and validations

4.1. Modal analysis

In the studies of hydroelasticity, both model tests and numerical simulations rely on the hull surface to obtain hydrodynamic forces from the fluid domain. However, it is important to note that the elastic responses are primarily experienced by the hull girder. Therefore, it is imperative to validate the congruity of mass and stiffness distribution of simplified hull girder with the real conditions. Modal analysis is often applied to calculate the 2-node and 3-node order natural frequencies of a simplified beam model and to validate with experimental data. In this study, the natural modes (seen in Fig. 11) and natural frequencies (seen in Table 3) of 2-node and 3-node modes are computed using the LAPACK solver in MBDyn. The obtained natural frequencies exhibit good agreement with experimental data.

4.2. Grid sensitivity study

In the present mesh sensitivity study, there are three sets of mesh grids (summarized in Table 4) are simulated to investigate the numerical uncertainties caused by computational mesh. The wave-structure condition of λ/L = 0.9 is selected for comparison because of the relative severe hydroelastic responses.

In sensitivity study, the Richardson extrapolation method is applied. The convergence rate R, computational precision P, extrapolated value S_{ext}, approximate relative error e_a, extrapolated relative error e_{ext}, and the *GCI* (Grid Convergence Index) are calculated as follows:

$$R = \frac{s_2 - s_1}{s_3 - s_2} = \frac{\varepsilon_{21}}{\varepsilon_{32}} \tag{19}$$

$$P = \frac{\left| ln \left| \frac{\varepsilon_{21}}{\varepsilon_{32}} \right| \right|}{ln r} \tag{20}$$

$$S_{ext,32} = \frac{r^p s_2 - s_3}{r^P - 1} \tag{21}$$

$$e_{a,32} = \frac{|s_3 - s_2|}{|s_2|} \tag{22}$$

$$e_{ext,32} = \frac{|s_{ext,32} - s_2|}{|s_{ext,32}|} \tag{23}$$

$$GCI = \frac{1.25 \times e_{a,32}}{r^P - 1} \tag{24}$$

Where s_1, s_2, and s_3 represents numerical prediction results of ship motions and VBM load under fine, medium and coarse mesh, respectively. $S_{ext,32}$ and $e_{a,32}$ are the extrapolated value and approximate
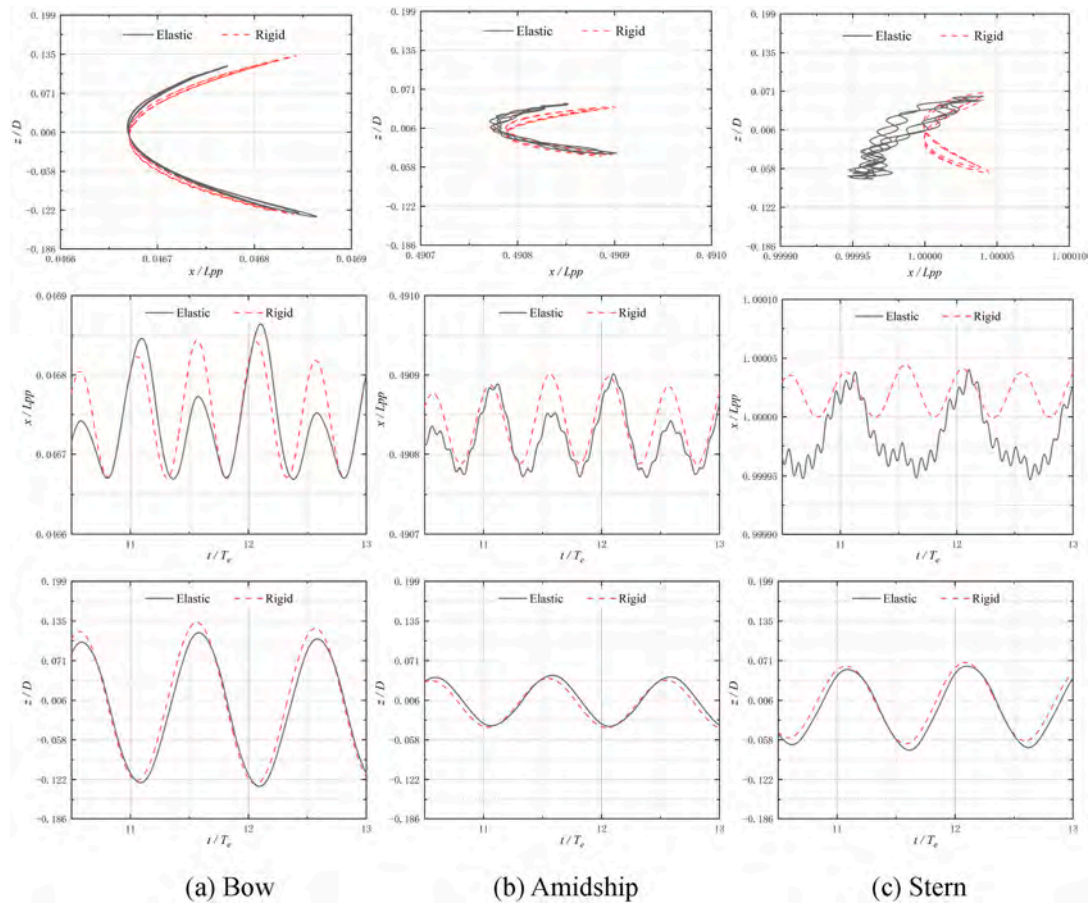
Fig. 24. Displacement trajectories and vibration time histories of typical nodes in ship beam (λ/L = 0.9).

relative error based on s_2 and s_3, respectively. Four convergence modes can occur according to the value of convergence ratio R: (i) monotonic convergence (MC) when $0 < R < 1$; (ii) oscillatory convergence (OC) when $-1 < R < 0$; (iii) monotonic divergence (MD) when $1 < R$; (iv) oscillatory divergence (OD) when $R < -1$. And the calculation of the uncertainty U depends on the convergence type. The uncertainty U is represented by *GCI* for the condition of MC, and is calculated with the following formula with the condition of OC:

$$U = \frac{1}{2}(s_{max} - s_{min}) \tag{25}$$

The time histories of heave and pitch motions, and VBM amidships are compared to using three different grid schemes, as illustrated in Fig. 12. The time series results of ship motions and VBM load show high degrees of consistency and the tendency of monotonic convergence. The verification parameters for grid size convergence study are demonstrated in Table 5. As shown in the table, the convergence type of MC is obtained for the motion and VBM predictions. All of the three grid schemes show good consistency, and the medium sized mesh is chosen as a compromise between computational accuracy and efficiency.

4.3. Experimental validation

The motion and VBM results are non-dimensionalized and compared with the experimental measurements and prediction results by potential theory, which both of the data come from CSSRC, as illustrated in Fig. 13 and Table 6. Compared with experimental data, the predictions of ship motion and VBM at midship show good agreement generally, except for slightly higher predicted results for midship VBM under two conditions of λ/L = 0.8 and λ/L = 0.9. Compared with the numerical simulation data by potential flow theory from CSSRC, it is noticed that the CFD results can overestimate the VBM load. As for the heave motion, Fig. 13 (a) shows that for the waves with small wavelength and period, the CFD predictions are higher than that by potential theory. And for the waves with large wavelength and period, the CFD results are smaller. It shows the similar characteristic between CFD and potential theory simulation results of heave motion by Lakshmynarayanana and Temarel (2020) and Jiao (2021).

From Fig. 15 (b) and (c), it can be observed that there exist strong interactions between the container ship and waves in the two conditions, resulting in an increase of the amplitude of high-order components in VBM loads. Combining Fig. 14 (b) and (c), wave-structure interaction induces a significant fourth-order harmonic component with large VBM amplitude, which confirms the phenomenon observed in Fig. 15. As mentioned earlier, this study assumes a zero structural damping to enhance the visibility of high order hydroelastic responses. However, neglecting the inhibitory effect of structural damping on vertical bending vibration of the hull girder may lead to an overestimation of amplitudes for high-order components, consequently causing an overestimation of predicted VBM loads as well. Statistically speaking, the relative errors between numerical predictions and experimental results for RAOs of VBM under the two conditions of λ/L = 0.8 and λ/L = 0.9 are found to be approximately 12.7% and 9.2%, while the VBM prediction errors for other conditions are within 5.0%. Overall, numerical calculations show good predictive accuracy.

5. Results and discussions

5.1. Wavelength effects

The effect of wavelength to VBM responses are compared and

discussed. The frequency domain spectra of the VBM responses at amidship under different wavelength conditions are shown in Fig. 14. The Fig provides the wave encounter frequency and the natural frequency of vertical bending vibration of 2-node order of the beam as references. In all cases, the peak frequency of the first harmonic load coincides with the wave encounter frequency. In some conditions, up to 5th harmonic responses are induced on the ship model, while at least 4th harmonic loads are detected in all situations. Except for the conditions of $\lambda/L = 0.8$ and $\lambda/L = 0.9$, the amplitudes of high-order harmonic loads are small. By setting a maximum value for the Young's modulus of the beam, the hydroelastic responses for a rigid ship is calculated under the condition of $\lambda/L = 0.9$, as shown in Fig. 14 (j). Compared to the VBM spectrum of an elastic ship, the highest order harmonic response that can be detected is 4th harmonic load for a rigid ship. Furthermore, the VBM amplitude of first harmonic load is a little bit higher for a rigid ship compared to an elastic one, with smaller amplitude of higher order harmonic load components. This indicates that hydroelastic responses for a rigid ship focus on the wave frequency (WF) component that coincides with wave encounter periods and have lower high frequency responses.

The time histories of VBM components at midship under different wavelength conditions from 15 s to 20 s are presented in Fig. 15. It can be observed that higher order harmonic components are relatively obvious at conditions of $\lambda/L = 0.8$ and $\lambda/L = 0.9$, while the total VBM exhibits significant differences compared to wave frequency VBM, with larger amplitude during this period. As the wavelength decreases below 0.8L or exceeds 0.9L, the responses of amidship VBM gradually become dominated by wave frequency response, and the total VBM becomes smoother and closer to wave frequency VBM.

The influence of WF and HF VBM components is quantitatively compared under different wavelengths. The VBM amplitudes and component proportions towards total VBM are summarized in Table 7. It's clear that the HF component proportions are over 20% for the conditions of $\lambda/L = 0.8$ and $\lambda/L = 0.9$. The minimum component proportion of WF VBM occurs in the condition of $\lambda/L = 0.9$ with the value higher than 85%. It means the WF component is dominant in total VBM for the wave conditions with relative small wave height. The influence of the HF components is obvious for the conditions of wavelength near $\lambda/L = 1.0$, but relative small for total VBM.

The longitudinal distribution of VBM obtained from calculations for different wave conditions is plotted as scatter points on Fig. 16 with the envelope lines. For all cases, the maximum value of hogging VBM occurs at the 10th segment, which is located at the amidship. The maximum value of sagging VBM occurs at both the 10th and 11th sections, which are near the midship and closer to its bow. The longitudinal distribution of VBM for different wave conditions exhibit similar trends. Additionally, the extreme value of sagging VBM is slightly larger than that of hogging VBM.

5.2. Structural stiffness effects

The effects of structural stiffness are studied by comparing the motion and VBM responses between rigid body and elastic ship under the same situation of $\lambda/L = 0.9$. The time histories of heave and pitch motions are illustrated in Figs. 17 and 18. The shape and amplitude of both cases show great agreement, except of the hysteresis phase of elastic results.

The longitudinal distribution of VBM for both rigid and flexible ships are compared under the case of $\lambda/L = 0.9$, as shown in Fig. 19. Compared to a rigid ship, the maximum response of VBM for a flexible ship is slightly larger, and there is a greater difference in response between sagging and hogging bending. The trend of the distribution of VBM for a flexible ship is similar to that of a rigid ship. Table 8 compares the RAOs of ship motion and VBM at amidship between rigid and elastic ships. The amplitude of VBM response is underestimated by using a rigid ship model in the numerical prediction.

Fig. 20 compares the time series of VBM components between rigid and flexible ships from 15 s to 20 s. The amplitudes of wave frequency component of VBM calculated by rigid and elastic ships are almost identical. However, elastic model shows a significant high order component, which is underestimated by rigid body, as shown in Table 9. This result is the same with the numerical simulation conclusions from Lakshmynarayanana and Temarel, 2020; Lakshmynarayanana and Hirdaris, 2020. In this study, the high order component of VBM is underestimated 73.0% compared to elastic ship, and the total VBM is underestimated 13.0%. Though there is little difference of the structural deformation acting to flow field, the vibration and dynamic responses of elastic beam cannot be ignored.

Four typical moments are selected to compare the motion of the elastic container ship and longitudinal distribution of VBM at different time in one wave encounter period, as shown in Fig. 21. T_e is the encounter period of ship motion. Due to low sea conditions, there is no phenomena of green water and slamming in the calculations for the ship model. From the relationship between waves and the position of ship, it can be observed that at each moment, the extreme values of VBM occur at the crest or trough positions of the waves. When the pitch motion of the ship reaches its maximum angle, the crest or trough of the wave happens to be located at midship position. Therefore, this moment corresponds to inducing either a maximum value for hogging VBM (wave crest at midship) or a minimum value for sagging VBM (wave trough at midship), respectively.

Fig. 22 shows the flow field and vortical structures around the ship at the time of 17.00 s. For the cases of rigid body and elastic ship, the distribution of wave height in the flow field exhibits remarkable similarity. The vortical structures are postprocessed by Liutex method, which has been proved as an effective way to identify vortex with high accuracy (Liu. et al., 2018; Zhao et al., 2020). Compared with the vorticity structures of rigid ship, the elastic one shows more intact vorticity structures, especially in the ship stern. However, in the macro level, there is negligible interference from the elastic deformation of ship on the flow field. Consequently, both elastic ship and rigid body demonstrate similar wave-frequency hydroelastic response amplitudes.

However, at smaller scales, little difference of local deformation distribution can be found between an elastic and a rigid body on the ship bow and stern, reflecting micro-amplitude vibration responses in the elastic hull beam, as shown in Figs. 23 and 24. At different time in one wave encounter period, the displacement distribution of elastic beam shows tiny difference with rigid one, especially when the peaks and troughs of waves in the amidship. The maximum ratio of vertical vibration of elastic beam to ship length between perpendiculars is 0.13%, meaning that the elastic vibration of the ship is small. In Fig. 24, the displacement trajectories of elastic ship nodes in bow, amidship, and stern are extracted and compared with that of rigid ship. The displacement trajectories of the elastic and rigid bow nodes show great similarity. However, the node displacement trajectory in ship stern shows strong nonlinearity. The comparison of nodal longitudinal and vertical displacement time histories between rigid and elastic ships show that the nonlinearity of displacement trajectories is mainly caused by the longitudinal vibration of elastic ship. The structural vibration leads to high frequency responses of VBM. It becomes the main difference of hydroelastic characteristics between elastic and rigid ships.

6. Conclusions

This paper presents a two-way coupled FSI framework to investigate the ship hydroelasticity characteristics of a 20,000 TEU containership model in regular head waves. The coupled CFD-MBD numerical tool is established, and OpenFOAM is chosen as the fluid solver, while the MBDyn is selected as the structure solver to solve the deformation of flexible hull structure. A two-way implicit solver of preCICE is implemented for robust coupling and to allow data communication between the fluid and structure solvers.

The modal analysis is firstly presented to evaluate the accuracy of the mass and stiffness distribution of the numerical hull girder with experiments. Then the grid sensitivity study is applied. And the numerical results of RAOs of ship motion and VBM at midship are validated with experimental data.

In different wavelength conditions, the longitudinal distribution of VBM trends is roughly the same, with maximum values appearing near the midship section under hogging and sagging conditions. In this study, the amplitudes of hogging and sagging are approximately equal. The hydroelastic responses of ultra-large container ships exhibits significant high-frequency resonance components at wave conditions $\lambda/L = 0.8$ and $\lambda/L = 0.9$, where VBM response also reaches its maximum value. All studied conditions in this paper involve small waves with small wave stiffness, resulting in no occurrence of green water or obvious slamming phenomena, thus leading to relatively fewer higher-order components in VBM response. A comparison between rigid and flexible ship hydroelastic responses reveals that the predicted VBM for flexible ships is slightly larger than that for rigid ships, suggesting that considering beam flexibility is necessary for flexible ships, especially ultra-large container ships.

In this paper, a series of regular wave conditions of 20,000 TEU containership are computed and validated with experimental data. In the future, more validations of different wave conditions and ship types will be investigated. Moreover, the hydroelastic responses of containerships in irregular waves, especially in extreme sea conditions are planning to be studied. Moreover, only the symmetrical structural responses are studied in this paper under head waves, the importance of antisymmetric effects of ships in oblique waves ought to be discussed in the future work.

CRediT authorship contribution statement

Wenjie Zhang: Writing – original draft, Visualization, Validation, Methodology, Investigation, Formal analysis, Data curation. **Jianhua Wang:** Writing – review & editing, Writing – original draft, Supervision, Software, Resources, Methodology, Investigation, Funding acquisition, Data curation, Conceptualization. **Hao Guo:** Validation, Investigation, Data curation. **Yi Liu:** Validation, Investigation, Data curation. **Decheng Wan:** Supervision, Software, Resources.

Declaration of competing interest

The authors declare that they have no known competing financial interests or personal relationships that could have appeared to influence the work reported in this paper.

Acknowledgements

References

Betts, C.V., Bishop, R.E.D., Price, W.G., 1977. The symmetric generalized fluid forces applied to a ship in a seaway. RINA Supplementary Papers 119 (269), 265–278.
Bishop, R.E.D., Price, W.G., 1979. Hydroelasticiy of Ships[M]. Cambridge University Press.
Faltinsen, O.M., Michelsen, F.C., 1975. Motions of Large Structures in Waves at Zero Froude number[J]. Classification and Registry of Shipping, p. 90.
Faltinsen, O., Zhao, R., 1991. Numerical predictions of ship motions at high forward speed. Philos. Trans. R. Soc. London, Ser. A 334, 241–252.
Fukasawa, T., 1990. Hydroelastic responses of a membrane structure in waves. International Symposium on the Dynamics of Marine Vehicles and Structures in Waves. Brunel University, Uxbridge, U.K., pp. 147–156
Ghiringhelli, G.L., Masarati, P., Mantegazza, P., 2000. A multi-body implementation of finite volumes C0 beams. AIAA J. 38 (1), 131–138.
Gu, M., Wu, Y., Xia, J., 1989. Time domain analysis of non-linear hydroelastic response of ships[C]. 4th International Symposium on Practical Design of Ships and Mobile Units (PRADS). Varna, Bulgaria.
Hermundstad, O.A., Aarsnes, J.V., Moan, T., 1999. Linear hydroelastic analysis of high-speed catamarans and monohulls. J. Ship Res. 43 (1), 48–63.
Hermundstad, O.A., Wu, M.K., Moan, T., 1994. Hydroelastic response analysis of a high speed monohull[C]. Hydroelasticity in Marine Technology, Faltinsen et al. Balkema, Rotterdam.
Huang, S., Jiao, J., Soares, C.G., 2022. Uncertainty analyses on the CFD–FEA co-simulations of ship wave loads and whipping responses. Mar. Struct. 82, 103129.
Inglis, R., 1981. The Influence of speed dependent boundary condition in three-dimensional ship motion problems. Int. Shipbuild. Prog. 28.
Jiao, J., Huang, S., Wang, S., et al., 2021. A CFD–FEA two-way coupling method for predicting ship wave loads and hydroelastic responses. Appl. Ocean Res. 117, 102919.
Jiao, J.L., Huang, S.X., Tezdogan, T., et al., 2021. Slamming and green water loads on a ship sailing in regular waves predicted by a coupled CFD-FEA approach. Ocean Eng. 241, 110107.
Korvin-Kroukovsky, B.V., Jacobs, W.R., 1957. Pitching and Heaving Motions of a Ship in Regular Waves kroukovsky.
Lakshmynarayanana, P.A., Temarel, P., 2020. Application of a two-way partitioned method for predicting the wave-induced loads of a flexible containership. Appl. Ocean Res. 96, 102052.
Lakshmynarayanana, P.A.K., Hirdaris, S., 2020. Comparison of nonlinear one- and two-way FFSI methods for the prediction of the symmetric response of a containership in waves. Ocean Eng. 203, 107179.
Liu, C.Q., Gao, Y.S., et al., 2018. Rortex - a new vortex vector definition and vorticity tensor and vector decompositions. Phys. Fluids 30 (3), 035103.
Liu, G.J., 2021. Research on the Nonlinear Ship Hydroelasticity Based on CFD-FEM Two-Way Coupling Method[D]. Dalian University of Technology, Dalian.
Lu, Y., Liu, J., Teng, B., et al., 2022. Modal investigation on a large-scale containership model for hydroelastic analysis. Shock Vib. 1–11, 2539870.
Masarati, P., Morandini, M., et al., 2014. An efficient formulation for general-purpose multibody/multiphysics analysis. J. Comput. Nonlinear Dynam. 9 (4), 041001.
MBDyn, 2017. MBDyn Input File Format Version 1.7.3.
Menter, F.R., 1994. Two-equation eddy-viscosity turbulence models for engineering applications. AIAA J. 32 (8), 1598–1605.
Newman, J.N., 1978. The theory of ship motions. Adv. Appl. Mech. 18, 221–283.
Oberhagemann, J., Moctar, O.E., Schellin, T.E., 2008. Fluid-Structure Coupling to Assess Whipping Effects on Global Loads of a Large containership[C]. Symposium on Naval Hydrodynamics.
Oberhagemann, J., Shigunov, V., Moctar, O., 2012. Application of CFD in long-term extreme value analyses of wave loads. Ship Technol. Res. 59 (3).
Paik, K.J., Carrica, P.M., Lee, D., et al., 2009. Strongly coupled fluid–structure interaction method for structural loads on surface ships. Ocean Eng. 36, 1346–1357.
Price, W.G., Temarel, P., Yousheng, W., 1985. Structural responses of a SWATH or multi-hull vessel travelling in waves[C]. SWATH Ships and Advanced Multi-Hulled Vessels. RINA, London.
Price, W.G., Wu, Y., 1989. The Influence of Non-linear Fluid Forces in the Time Domain Responses of Flexible SWATH Ships Excited by a Seaway, vol. 2. OMAE, pp. 125–135.
Salvesen, N., 1970. Ship Motions and Sea loads[J]. SNAME transaction.
Seng, S., 2012. Slamming and Whipping Analysis of ships[D]. Technical University of Denmark, Copenhagen.
Simeon, B., 2006. On Lagrange multipliers in flexible multibody dynamics. Comput. Methods Appl. Mech. Eng. 195, 6993–7005.
Takami, T., Iijima, K., 2020. Numerical investigation into combined global and local hydroelastic response in a large container ship based on two-way coupled CFD and FEA. J. Mar. Sci. Technol. 25, 346–362.
Takami, T., Matsui, S., Oka, M., et al., 2018. A numerical simulation method for predicting global and local hydroelastic response of a ship based on CFD and FEA coupling. Mar. Struct. 59, 368–386.
Wang, J.H., Zhao, W.W., et al., 2019. Development of naoe-FOAM-SJTU solver based on OpenFOAM for marine hydrodynamics. J. Hydrodyn. 31 (1), 1–20.
Wang, J.H., Zou, L., et al., 2018. Numerical simulations of zigzag maneuver of free running ship in waves by RANS-overset grid method. Ocean Eng. 162, 55–79.
Wang, J.H., Zou, L., et al., 2017. CFD simulations of free running ship under course keeping control. Ocean Eng. 141, 450–464.
Wei, Y., Incecik, A., Tezdogan, T., 2023. A hydroelasticity analysis of a damaged ship based on a two-way coupled CFD-DMB method. Ocean Eng. 274, 114075.
Wei, Y., Yu, S., Jin, P., et al., 2024. Coupled analysis between catenary mooring and VLFS with structural hydroelasticity in waves. Mar. Struct. 93, 103516.
Wei, Y.J., Incecik, A., Tezdogan, T., 2022. A fully coupled CFD-DMB approach on the ship hydroelasticity of a containership in extreme wave conditions. J. Mar. Sci. Eng. 10, 1778.
Wu, Y.S., Maeda, H., Kinoshita, T., 1997. The Second Order Hydrodynamic Actions on A Flexible Body. Tokyo.
Xiao, J.W., Liu, C., et al., 2024. A two-way coupled fluid-structure interaction method for predicting the slamming loads and structural responses on a stiffened wedge. Phys. Fluids 36, 077123.
Yang, P., Feng, Q., Chen, H., et al., 2021. Combined backbone application on numerical simulations and a model experiment of a 20,000 TEU container ship. Ocean Eng. 223, 108662.
Zhao, W.W., Wang, J.H., et al., 2020. Vortex identification methods in marine hydrodynamics. J. Hydrodyn. 32 (2), 286–295.